

Reliability of DC-link capacitor in pulsed power supply for accelerator magnet*

Jie Wang,^{1,2,3} Da-Qing Gao,^{1,3} Wan-Zeng Shen,¹ Hong-Bin Yan,^{1,3,†} and Li-Jun Mao^{1,3}

¹*Institute of Modern Physics, Chinese Academy of Sciences, Lanzhou 730000, China*

²*School of Nuclear Science and Technology, Lanzhou University, Lanzhou 730000, China*

³*School of Nuclear Science and Technology, University of Chinese Academy of Sciences, Beijing 100049, China*

Capacitors are widely used in pulsed magnet power supplies to reduce ripple voltage, store energy, and decrease power variation. In this study, DC-link capacitors in pulsed power supplies were investigated. By deriving an analytical method for the capacitor current on the H-bridge topology side, the root-mean-square value of the capacitor current was calculated, which helps in selecting the DC-link capacitors. The proposed method solves this problem quickly and with high accuracy. The current reconstruction of the DC-link capacitor is proposed to avoid structural damage in the capacitor's current measurement, and the capacitor's hot spot temperature and temperature rise are calculated using the FFT transform. The test results showed that the error between the calculated and measured temperature increases was within 1.5 °C. Finally, the lifetime of DC-link capacitors was predicted based on Monte Carlo analysis. The proposed method can evaluate the reliability of DC-link capacitors in a non-isolated switching pulsed power supply for accelerators and is also applicable to film capacitors.

Keywords: Aluminum electrolytic capacitor, DC-link current, DC-DC power converter, Hot spot temperature

I. INTRODUCTION

With the development of proton synchrotrons [1–3] and heavy-ion accelerators [4–6], the repetition cycle of the beam has shortened. The beam must be accelerated to high energy quickly, so the pulsed power supply must have a fast current rise rate and high tracking accuracy [7]. The magnet and magnetic excitation power supply constitute a magnetic field system, one of the accelerator's main components. The pulsed power supply requires a high-precision current and a wide range of high voltages, and the output power is very large. Morita et al. [1] introduced the main-ring (MR) power supply for the Japan Proton Accelerator Research Complex (J-PARC). An energy storage device composed of capacitor banks (CBs) was studied to suppress the power variation in the electrical system. Peron et al. [2, 3] reported a new power supply for the CERN proton-synchrotron (PS) accelerator based on three-level converters with capacitive energy storage. The DC-link capacitor banks between AFE and the DC/DC converters store and exchange energy with the magnets. The reliability of the pulsed power supply transforms into the reliability of power devices, which is an extensive study topic [8–10] and that of the Aluminum electrolytic capacitor [11, 12].

Aluminum electrolytic capacitors have long been widely used in power electronic equipment owing to their large capacitance and low cost. DC-link capacitors are essential components that compensate for the instantaneous power difference between the front and rear ends of the power converter and reduce the voltage ripple. They are considered one of the most fragile parts of power electronic systems [13], affecting the volume and reliability of power supplies. In general, three types of capacitors are used in DC-link applications: Met-

allized Polypropylene Film Capacitors (MPPF-Caps), Aluminum Electrolytic Capacitors (Al-Caps), and multilayer ceramic capacitors (MLC-Caps) [11]. The design of a DC-link capacitor must consider the ripple current of the capacitor. The current calculation of the capacitor root-mean-square (RMS) can effectively guide the capacitor selection and avoid volume and weight oversizing. Ahmad et al. [14] evaluated the DC-link capacitor RMS current of a switched reluctance motor (SRM) drive. Huang et al. [15] calculated the ripple current in a DC-link capacitor for brushless DC motor (BLDCM) square-wave control system. Kolar et al. [16] derived a simple analytical expression for the current stress on a DC-link capacitor caused by the load-side inverter of a voltage DC-link converter system. This expression is widely used in the calculation of DC-link capacitor RMS calculation in many inverters, but it is not applicable to DC/DC converters. Therefore, this study derives an analytical expression for the RMS value of the DC-link capacitor current based on the topological states of the pulsed power supply.

Hotspot temperature is a significant factor that affects the capacitor's lifetime. Capacitor hot spot temperature calculation methods include finite element simulation [20], measured directly by using a thermocouple [19] or optocoupler [21], or using an infrared camera (IR camera) [17]; The measurement method based on the IR camera can only measure the case temperature, but cannot obtain the internal temperature; The finite element simulation needs to establish three-dimensional geometric modeling inside the capacitor and provide the external dimensions and thermal characteristics parameters of the corresponding materials. Capacitor manufacturers usually do not provide these parameters, which are difficult to achieve, and the accuracy is sometimes questioned. In some studies, the temperature analysis of the capacitor was verified through the case temperature, which lacked the direct verification of hotspot temperature measurements. The hotspot temperature was directly measured, and the experimental results were found to be more reliable.

The lifetime of an aluminum electrolytic capacitor is

* This work was supported by the National Key Research and Development Program of China (No. 2019YFA0405402).

† Corresponding author, yanhb@impcas.ac.cn

mainly determined by the ambient temperature and ripple current, and a low lifetime is a major constraint [22]. Thermal stress is a key factor in capacitor wear, leading to a shortened lifetime [11]. In grid-connected Photo Voltaic (PV) systems, Yang et al. [21] translated real-field mission profiles (i.e., solar irradiance and ambient temperature) into the voltage, current, and temperature stresses of DC capacitors under both normal and abnormal grid conditions. For metro traction drive systems, the DC-link capacitor current harmonics of multiple operating conditions and different control methods have been discussed to evaluate the hotspot temperature and case temperature [20]. Combined with the analysis of electrical and thermal stresses, a multi-timescale capacitor reliability evaluation method was proposed. Wang et al. [23] presented the lifetime estimation of DC-link capacitors in Adjustable speed drives (ASDs); under balanced and unbalanced grid voltage conditions, a reliability evaluation method with long-term mission profile is proposed. The reliability of capacitors has also been investigated from several perspectives, such as condition monitoring [24, 25] and accelerated testing [19]. In this study, the reliability of capacitor banks was evaluated based on hotspot temperature under pulsed power supply applications.

An analytical calculation of the RMS value of the DC-link capacitor current is presented in detail in the following section. Section 3 outlines the hotspot temperature, considering current reconstruction and electrothermal coupling. In Sect. 4, we present the experimental verification of the capacitor current RMS value and hotspot temperature, and the results demonstrate the effectiveness of the proposed method. Section 5 describes the lifetime prediction of capacitor banks under different conditions using a Monte Carlo analysis.

II. ANALYTICAL CALCULATION OF THE CAPACITOR CURRENT RMS VALUE

A. Topology of pulsed power supply

The typical topology of a non-isolated switching-pulsed power supply is shown in Fig. 1, which consists of a front-end voltage source V_{dc} , DC-link capacitors C , IGBT modules S1-S4, and a resistance-inductance load R - L . The front voltage source provided a DC voltage that satisfied the power and voltage ripple requirements of the rear stage. In low-power situations, many programmable DC power supply products are used as the front voltage source with single-phase rectifier circuits; in medium- or high-power applications, commonly used circuits include three-phase uncontrolled rectifiers, three-phase bridge thyristor rectifiers, and three-phase PWM rectifiers. H-bridge choppers are divided into types A, D, and E, corresponding to the one-, two-, and four-quadrant operating modes, respectively [26]. This article discusses a D-type chopper with a positive load current and positive or negative load voltage. In the descending section of the pulsed current, the load voltage may be negative owing to the load inductance. In this figure, i_c denotes the capacitor current, i_1 is the output current of the front-end voltage source, and i_2 is

the input current of the H-bridge.

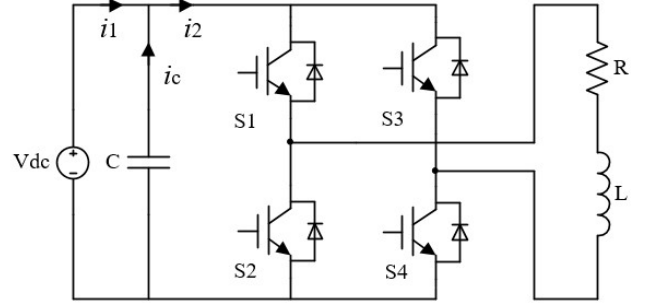


Fig. 1. The typical H-bridge topology of non-isolated switching pulsed power supply for accelerator.

The DC-link capacitor current i_c is obtained as

$$i_c = i_2 - i_1 \quad (1)$$

i_1 and i_2 can be decomposed into DC and AC components as follows:

$$i_1 = I_{1,avg} - i_{1,ac}, \quad i_2 = I_{2,avg} - i_{2,ac} \quad (2)$$

where $I_{1,avg}$ and $I_{2,avg}$ denote the DC components of i_1 and i_2 , respectively; $i_{1,ac}$ and $i_{2,ac}$ represent the AC components of i_1 and i_2 , respectively. The capacitor ripple current is defined as the AC current flowing through a capacitor. Therefore, instead of Eq. (1), i_c is expressed as follows:

$$i_c = i_{2,ac} - i_{1,ac} \quad (3)$$

The RMS value of the capacitor current $I_{c,rms}$ can be obtained from [16]:

$$I_{c,rms}^2 = I_{1,ac,rms}^2 + I_{2,ac,rms}^2 \quad (4)$$

where $I_{1,ac,rms}$ and $I_{2,ac,rms}$ are the RMS values of the i_1 and i_2 AC components, respectively. The capacitor RMS current is composed of the output current of the front-end voltage source and the current component caused by the H bridge. When the front-end is a voltage source, $I_{1,ac,rms}$ can be ignored, and only the current caused by the H-bridge can be calculated, $I_{c,rms} = I_{2,ac,rms}$, Eq. (4) can be simplified as follows:

$$I_{c,rms}^2 = I_{2,ac,rms}^2 = I_{rms}^2 - I_{avg}^2 \quad (5)$$

where I_{rms} denotes the DC-link RMS current and I_{avg} represents the DC-link average current.

B. Calculation of DC-link capacitor RMS current

The reference current patterns are shown in Fig. 2, where the pulsed current has two DC regions at 10 A and 300 A, flat top and flat bottom, which are used for beam injection and extraction, respectively. The reference current increases from

0 to the flat-bottom value, increases to the flat-top value, and then decreases to 0 with different slopes. The parameters of the current waveform are listed as: the rising time and falling time are 0.128 s, the flat top current is 300 A or 500 A, the flat bottom current is 10 A, the flat top time and the flat bottom time are 10 ms and 2 ms respectively, and the current period is 0.396 s. The pulsed power supply repeatedly outputs current.

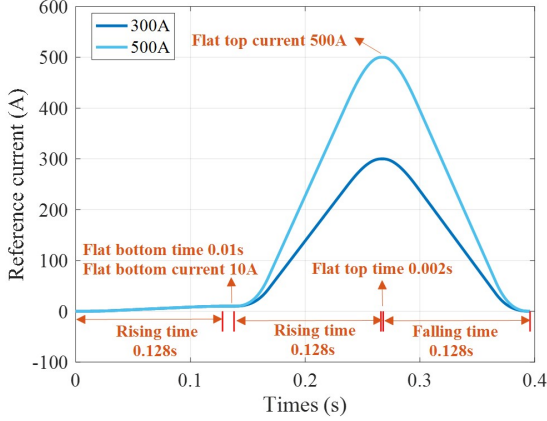


Fig. 2. Reference current pattern.

The load voltage of a pulsed power supply is related to the load parameters, current value, and current rate of increase. Based on the characteristics of the resistive load, the load voltage V_{load} can be described as [27]

$$V_{load} = L \frac{dI_{ref}}{dt} + I_{ref}R, \quad (6)$$

where I_{ref} denotes the reference current and dI_{ref}/dt represents the slope of the reference current pattern, R and L represent resistance and inductance, respectively. The H-bridge operates in the double-frequency chopping mode, and the IGBT duty ratio D can be expressed as

$$D = \frac{\frac{V_{load}}{V_{dc}} + 1}{2}, \quad (7)$$

where V_{dc} denotes the DC-link voltage. When the power supply is working, switches S1 and S4 and the freewheeling diodes work in parallel with them. The power supply outputs pulsed or direct current. When the duty ratio of IGBT is greater than 50%, switches S1 and S4 have a common conduction time, in which the energy flows to the magnet load from the front stage with frequency doubling and chopping;

when the duty ratio of IGBT is less than 50%, there is no time for S1 and S4 to conduct together, and the energy is fed back from the load to the front stage. The output duty ratio D_o is defined as

$$D_o = \frac{V_{load}}{V_{dc}}. \quad (8)$$

The output duty ratio is analyzed in the following section. During the switching cycle, the power supply switched between different states. Figure 3 presents the four operating states. State a indicates that the energy flows from the front stage to the magnet, states b and c are in a freewheeling state, and state d indicates that the energy of the magnet is fed back to the front stage. When $V_{load} > 0$, i.e. $D_o > 0$, the operating state is switched between the states a, b, and c, and When $V_{load} < 0$, i.e. $D_o < 0$, the working state is switched between the states d, b, and c.

To analyze the current in the circuit under different operating conditions, assuming that the initial voltage of the capacitor is M and the initial current of the inductor is N , and based on the Laplace transform, some circuit equations are listed to solve the inductor current under state a. The inductor current i_L and input current of the H-bridge i_2 can be obtained as

$$\begin{aligned} i_L(t) &= \mathcal{L}^{-1} \left[\frac{N}{(s + R/L)} + \frac{V_{dc}/L}{s(s + R/L)} \right] \\ &= N \cdot e^{-\frac{R}{L}t} + \frac{V_{dc}}{R} \left(1 - e^{-\frac{R}{L}t} \right) \\ i_2(t) &= i_L(t) \end{aligned} \quad (9)$$

i_L and i_2 in states b and c are expressed as

$$\begin{aligned} i_L(t) &= \mathcal{L}^{-1} \left[\frac{N}{(s + R/L)} \right] = N \cdot e^{-\frac{R}{L}t} \\ i_2(t) &= 0 \end{aligned} \quad (10)$$

i_L and i_2 under state d are given by

$$\begin{aligned} i_L(t) &= \mathcal{L}^{-1} \left[\frac{N}{(s + R/L)} - \frac{V_{dc}/L}{s(s + R/L)} \right] \\ &= N \cdot e^{-\frac{R}{L}t} - \frac{V_{dc}}{R} \left(1 - e^{-\frac{R}{L}t} \right) \\ i_2(t) &= -i_L(t) \end{aligned} \quad (11)$$

In summary, the expression for the input current of the H-bridge i_2 is:

$$\begin{aligned} i_2(t) &= \begin{cases} N \cdot e^{-\frac{R}{L}t} + \frac{V_{dc}}{R} \left(1 - e^{-\frac{R}{L}t} \right), & 0 < t < D_o T; \\ 0, & D_o T < t < T; \end{cases} & D_o(t) > 0; \\ i_2(t) &= \begin{cases} -N \cdot e^{-\frac{R}{L}t} + \frac{V_{dc}}{R} \left(1 - e^{-\frac{R}{L}t} \right), & 0 < t < |D_o T|; \\ 0, & |D_o T| < t < T; \end{cases} & D_o(t) < 0; \end{aligned} \quad (12)$$

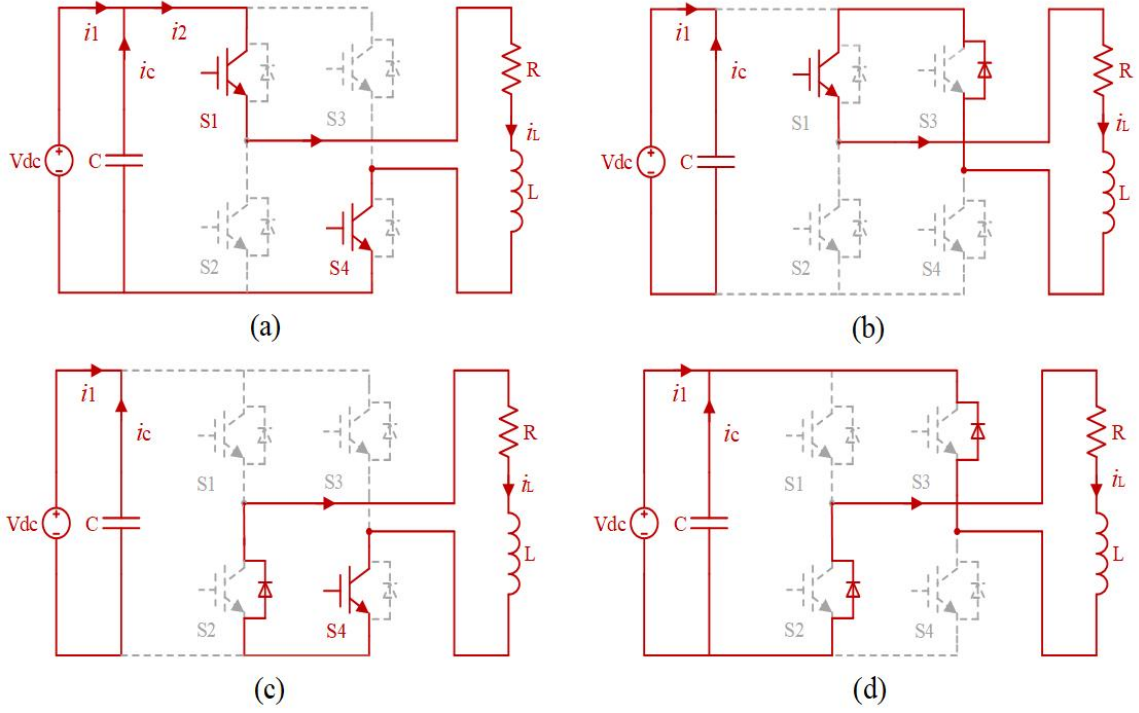


Fig. 3. The operation status of the H-bridge topology.

where T is the period after frequency doubling, which is equal to $1/2f_s$, f_s denotes the switching frequency. The DC-link RMS current I_{rms} and DC-link average current I_{avg} are given by

$$\begin{cases} I_{rms} = \sqrt{\frac{1}{T} \int_0^T (i_2)^2 dt} \\ I_{avg} = \frac{1}{T} \int_0^T i_2 dt \end{cases} \quad (13)$$

Combining Eq. (5), the capacitor RMS current $I_{c,rms}$ is obtained as follows:

$$I_{c,rms} = \sqrt{I_{rms}^2 - I_{avg}^2} \quad (14)$$

III. THE HOT SPOT TEMPERATURE CALCULATION

A. Capacitor current reconstruction

In practical pulsed power supply applications, capacitors are usually connected through stacked busbars, making it difficult to measure the current flowing through a DC-link capacitor using a current sensor. If a current sensor is installed, it damages the main circuit structure. To solve this problem, this study proposes a capacitor ripple current reconstruction method for pulsed power supplies.

The accelerator power supply requires minimal voltage ripple and extremely high current accuracy, LC filters are also added to the chopper output stage. By designing the filter and increasing the switching frequency, the output current index

can be further improved and ultimately meet the requirements of the accelerator power supply outputs. A schematic of the pulsed power supply is shown in Fig. 4, where L_f and C_f represent the filter inductance and capacitance, respectively, which reduce the voltage and current ripples, i_o and V_o are the current and voltage at the bridge output point, respectively.

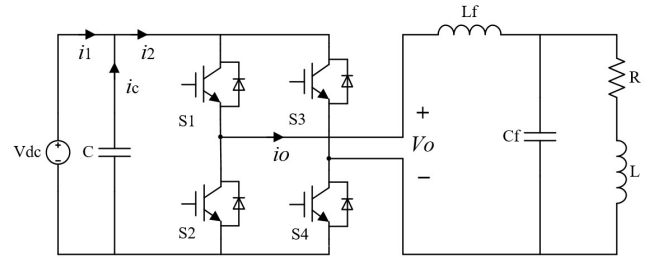


Fig. 4. The Schematic diagram of power supply.

i_c is determined using i_1 and i_2 . i_1 can be measured using current sensors. i_2 cannot be measured because of the practical connections of the stacked busbar. When the H-bridge is in state a, i_2 is equal to i_o ; When the H-bridge is in states b and c, i_2 equals zero; and When the H-bridge is in state d, i_2 equals $-i_o$. Therefore, i_2 is reconstructed using i_o .

In addition, the H-bridge states can be reflected by V_o , where V_o is equal to V_{dc} in state a, V_o is equal to 0 in states b and c, V_o is equal to $-V_{dc}$ in state d.

Due to $i_c = i_2 - i_1$, i_c can be reconstructed. Table 1 presents the principles of capacitor ripple current reconstruction. The

capacitor current can be reconstructed based on these principles.

Table 1. DC-link capacitor current reconstruction scheme.

States	H-bridge switch in "ON" state	V_o	i_2	i_c
a	S1,S4	V_{dc}	i_o	$i_o - i_1$
b	S1	0	0	$-i_1$
c	S4	0	0	$-i_1$
d	—	$-V_{dc}$	$-i_o$	$-i_o - i_1$

B. Thermal model of capacitor

An equivalent model of an aluminum electrolytic capacitor is shown in Fig. 5, where ESR denotes the equivalent series resistance, L is the equivalent series inductance, and C is the capacitance. The impedance Z_c of the capacitor is expressed as follows [21]:

$$Z_c = ESR + j2\pi fL + \frac{1}{2\pi fC}, \quad (15)$$

where f denotes the frequency. This indicates that the impedance is dominated by capacitance C in the low-frequency range, ESR in the mid-frequency range, and L in the high-frequency range. ESR varies with frequency. The thermal characteristics of a capacitor can be modeled using a thermal network, as shown in Fig. 5, where R_{thhc} is the thermal resistance from the hotspot to the case, R_{thca} is the thermal resistance from the case to the ambient environment, and R_{th} is the total thermal resistance, $R_{th} = R_{thhc} + R_{thca}$. T_h , T_c , and T_a are the hotspot, case, and ambient temperatures, respectively [28]. During operation, the capacitor current I_{rms} causes a power loss owing to the equivalent series resistance.

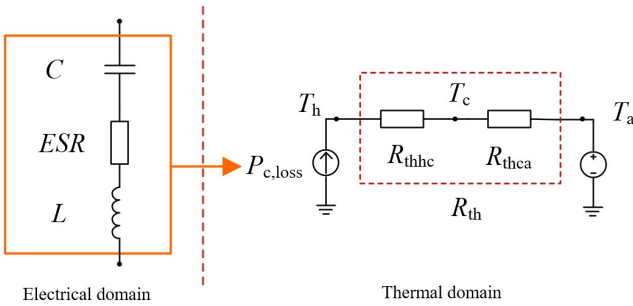


Fig. 5. The electrical and thermal models of aluminum electrolytic capacitor.

The heat in a capacitor is mainly generated by power loss, which is closely related to the ESR and ripple current. The capacitor current varied with the operating conditions of the power supply. The frequency spectrum of the capacitor ripple current was analyzed using FFT combined with ESR at different frequencies, and the power loss $P_{c,loss}$ can be expressed

as [21]

$$P_{c,loss} = \sum_{i=1}^n ESR(f_i) \times I_{rms}^2(f_i) \quad (16)$$

where $ESR(f_i)$ is the ESR of the capacitor at frequency f_i ; $I_{rms}(f_i)$ is the RMS value of the capacitor ripple current at frequency f_i ; and n is the number of frequency components.

An aluminum electrolytic capacitor (CECTN, FE50400103M5D5D1) was tested as the research subjects. The size of the capacitor is 91 mm×130 mm (diameter×height); the rated voltage and capacitance is 400 V, 10 000 μ F; the ESR is 12 m Ω (20 $^{\circ}$ C, 120 Hz). The thermal resistance R_{th} provided by the manufacturer was 2.75 K/W. Since the ESR varies with frequency, the capacitor manufactures normally specify a term called "Ripple Current Coefficient" F_{fi} and is expressed as:

$$F_{fi} = \sqrt{\frac{ESR(f_0)}{ESR(f_i)}}, \quad (17)$$

where f_0 is the rated frequency, usually at 120 Hz, $ESR(f_0)$ is the ESR of the capacitor at 120 Hz, $ESR(f_0) = 12$ m Ω . Table 2 lists the F_{fi} values for the capacitor ESR characteristics.

Table 2. Ripple current coefficients of the capacitor.

Frequency (Hz)	Rated current coefficient F_{fi}
2.5	0.32
120	1
300	1.15
1000	1.21
10k	1.12
20k	1.06

Combining Eq. (16), and Eq. (17), the power loss $P_{c,loss}$ is given by

$$P_{c,loss} = \sum_{i=1}^n I_{rms}^2(f_i) \times \frac{1}{F_{fi}^2} \times ESR(f_0) \quad (18)$$

The temperature increase ΔT at the center of the capacitor is given by

$$\Delta T = P_{c,loss} \times R_{th} \quad (19)$$

The hotspot temperature of DC-link capacitor T_h is obtained as follows:

$$T_h = T_a + \Delta T, \quad (20)$$

where T_a represents the ambient temperature.

Considering the $P_{c,loss}$ calculation under the condition of 0.05 F capacitance and a pulsed current of 500 A as an example, Table 3 lists the $P_{c,loss}$ solution process. The data for f_i and $I_{rms}(f_i)$ are presented in Figs. 9(c), which were obtained through FFT of the capacitor current. We consider the

frequencies, including low frequency 2.5 Hz, switching frequency 2, 4, 6, ..., and 16 times. An important harmonic current component of the capacitor, 2.5 Hz, is the frequency of the pulsed current. In the relationship between ESR and frequency, the frequency belongs to the area of extremely low frequency, and the ESR at 2.5 Hz was obtained by fitting. The ripple current correction coefficient parameter at 2.5 Hz was 0.32. In the hotspot temperature calculation for the capacitor, the maximum contribution was the RMS current at 2.5 Hz. The power loss $P_{c,loss}$ was 13.24 W, and the estimated temperature increase ΔT was 36.4 °C.

Table 3. A calculation case of $P_{c,loss}$.

i	f_i (Hz)	$I_{rms}(f_i)$ (A)	F_{fi}	$P_{c,loss}(f_i)$ (W)
1	2.5	10.19795	0.32	12.18728
2	18997.5	8.93195	1.06	0.85204
3	37997.5	2.9364	1.06	0.09209
4	57000	2.0438	1.06	0.04461
5	76000	1.3358	1.06	0.01906
6	95000	1.3703	1.06	0.02005
7	114000	0.8775	1.06	0.00822
8	133000	1.0056	1.06	0.01080
9	152000	0.7002	1.06	0.00524
$P_{c,loss}=13.24$ W, $\Delta T = P_{c,loss} \times R_{th} = 13.24 \times 2.75=36.4$ °C				

IV. EXPERIMENTAL VERIFICATION

A pulsed power supply experimental platform was established as shown in Fig. 6. The front-stage voltage source module is a PDB 400 V/100 A power supply that provides DC-link voltage and charges DC-link capacitor. The capacitor bank value was designed as 0.09 F/400 V or 0.05 F/400 V, consisting of nine or five capacitors placed in parallel and fixed on a stacked busbar. Two half-bridge IGBT modules (FF1400R17IP4) constitute the H-bridge. After the $L_f - C_f$ low-pass filter, a solenoid corresponding to inductor L in series with resistance R is used as the load. The gate signals of S1 and S4 were controlled by pulse-width modulation (PWM), whereas S2 and S3 were invariably closed, and their antiparallel diode freewheeling was utilized. The two IGBT modules were placed on a high-efficiency water-cooled heatsink. The specifications of the experimental setup are listed in Table 4.

Table 4. Experimental parameters.

Parameters	Value
Switching frequency f_s (kHz)	9.5
DC-link voltage V_{dc} (V)	200
DC-link capacitor C (F)	0.09
Filter capacitor C_f (μ F)	75
Filter inductance L_f (mH)	0.1
Load resistance R ($m\Omega$)	43
Load inductance L (mH)	10

A laminated busbar is a multilayer compacted connection between power electronic devices that minimizes stray induc-

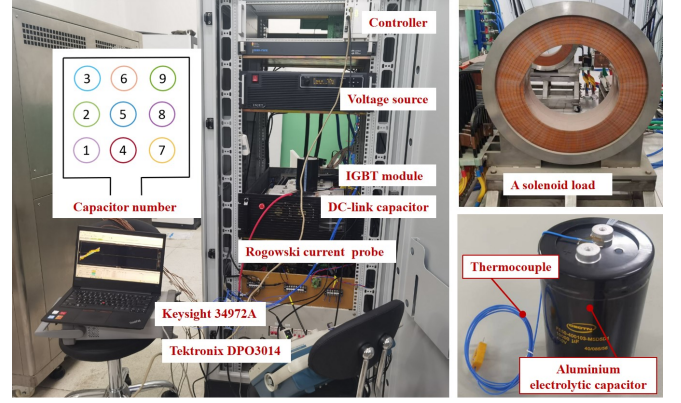


Fig. 6. (Color online) Pulsed power supply experimental platform and a sample of aluminum electrolytic capacitor with embedded thermocouple.

tance in the circuit and reduces overvoltage while the IGBT turns off. It is not convenient to measure the capacitance current directly when laminated busbar connections are used. The capacitor of the DC-link capacitor bank was extended to the connecting wire using copper bars, and a Rogowski Coil CWT6B probe was used to measure the capacitor ripple current. The temperature of the capacitor was measured using a type-K thermocouple sensor integrated into the internal center of the capacitor with an accuracy of ± 1.5 °C. Figure 6 shows a sample aluminum electrolytic capacitor with an embedded thermocouple. All capacitors in the DC-link capacitor bank were equipped with a thermocouple to measure the temperature. The thermocouple was connected to a multichannel data logger keysight 34972A to obtain the hotspot temperature of the capacitor. Two DCCTs were used to measure the current at the bridge output point and the current of the front-end voltage source, and a high-voltage probe was used to measure the load voltage.

A. Verification of DC-link capacitor RMS current

This section presents the analytical calculation of the capacitor RMS current in Sect. 2. The RMS value of the capacitor current can be obtained by calculating the RMS value of the AC component i_2 . According to Eq. (9) into Eq. (11), the waveform of i_2 can be analytically calculated. In addition, the waveform of i_2 can be obtained by establishing a simulation model using a simulation software. The capacitor current waveform i_{cap} could also be measured on the experimental platform.

Figure 7 shows the simulation, experiment, and analytical calculation of a single-capacitor current waveform at a pulsed current of 300 A and a DC-link capacitance of 0.09 F. The simulation waveform is the waveform of i_2 obtained using the simulation model. The experimental waveform is the waveform of the AC component of the capacitor current measured by the current probe, and the waveform of the proposed method is the waveform of i_2 obtained by analytical

calculation. The analytical calculation results for the capacitor current are consistent with the experimental results. The DC component of i_2 in the simulation was $I_{2,avg}=0.8786$ A, and the DC component of i_2 for the analytical calculations is $I_{2,avg}=0.8979$ A. The two i_2 values are shown in Fig. 7. DC-link capacitors are discharged during the rapid rise in current and charged in the rapidly falling section of the current.

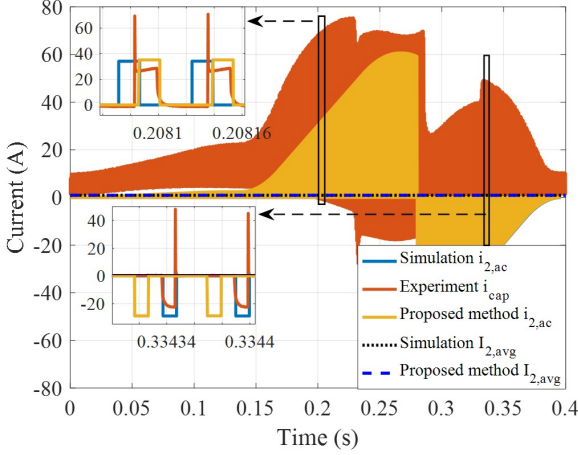


Fig. 7. (Color online) Experiment, simulation, and analytical calculation waveform of a capacitor.

From these three current waveforms, we obtained the current RMS values. Table 5 lists the RMS values of the capacitor currents obtained from the experiment, simulation, and the proposed method under different DC-link capacitances and pulsed currents. The proposed method values represent the RMS value of the AC component of i_2 obtained by the analytical calculation, that is, $I_{c,rms} = I_{2,ac,rms}$, the simulation values are the RMS values of the AC component of i_2 obtained by simulation, and the experimental values are the RMS values of the AC components of the measured capacitor current. The errors in the experimental results were within 1.27 A, proving that the proposed method is effective and accurate.

Table 5. Capacitor RMS current obtained from proposed method, experiment, and simulation in different reference current.

		300 A	400 A	500 A
0.05F	Proposed method $I_{2,ac,rms}$	12.51	16.60	19.90
	Experiment $I_{cap,rms}$	12.81	17.76	21.31
	Simulation $I_{2,ac,rms}$	12.71	16.87	20.04
	Error(exp.-mod.)	0.3	1.16	1.27
0.09F	Proposed method $I_{2,ac,rms}$	7.22	—	12.02
	Experiment $I_{cap,rms}$	7.54	—	13.24
	Simulation $I_{2,ac,rms}$	7.30	—	12.16
	Error (exp.-mod.)	0.32	—	1.22

B. Experimental verification of the hot spot temperature

Figure 8 shows the measured capacitor current and voltage waveforms for different pulsed currents and numbers of DC-

link capacitors. According to the experimental results, in the current rising stage from the flat base to the flat top, DC-link capacitors discharge and provide energy to raise the load current; and in the current falling stage from the flat-top to the 0-value, the capacitor is charged to store the energy feedback from the load.

Figure 9 shows FFT plots of the capacitor ripple current. The frequency spectrum plots show that the harmonic component is concentrated at two, four, and six times the switching frequency, consistent with frequency-doubling chopping. The larger the output pulsed current and the fewer the capacitors connected in parallel, the higher the RMS harmonic component of the capacitor current.

The curves of the hotspot and ambient temperatures of the Al-Cap under different conditions are shown in Fig. 10. An increase in the capacitor ripple current increases the capacitor temperature. The hotspot temperature stabilized after 6 h of operation, and the average temperature of the last 100 s was adopted as the experimental result to eliminate errors caused by fluctuations. The temperature rise results under different conditions are shown in Table 6. At a capacitance of 0.09 F, the maximum error value of the capacitor temperature rise was $\pm 0.4^\circ\text{C}$, and at a capacitance of 0.05 F, the maximum error value was $\pm 1.5^\circ\text{C}$. This proves that the method can effectively evaluate the hotspot temperature and temperature rise of DC-link capacitors. The temperature rise results calculated using the reconstructed and measured capacitor currents were consistent, indicating that the reconstructed current can be used to calculate the temperature rise efficiently.

In addition, the number of capacitors decreased from nine to five, and the experimental temperature rise at the 500 A current increased from 13.1°C to 34.9°C , which shows that reducing the capacitance by half will result in a significant increase in the hotspot temperature.

V. LIFETIME PREDICTION OF DC-LINK CAPACITOR BANKS

A. Monte Carlo Analysis and lifetime prediction

A block diagram of the lifetime evaluation of a DC-link capacitor is shown in Fig. 11, which consists of two parts. The first part comprises an analysis of electric and thermal stresses. Based on the different pulsed currents, the current stress of the DC-link capacitor was obtained and used as the input for the power loss model. The hotspot temperatures were calculated using a thermal model. The second part involved a Monte Carlo simulation and lifetime prediction considering parameter fluctuations.

For aluminum electrolytic and film capacitors, the lifetime model is expressed as follows [11]:

$$L = L_0 \times \left(\frac{V}{V_0} \right)^{-p_1} \times 2^{\frac{T_0 - T_h}{p_2}}, \quad (21)$$

where L_0 is the rated lifetime under the rated temperature T_0 and rated voltage V_0 , L is the actual lifetime under the

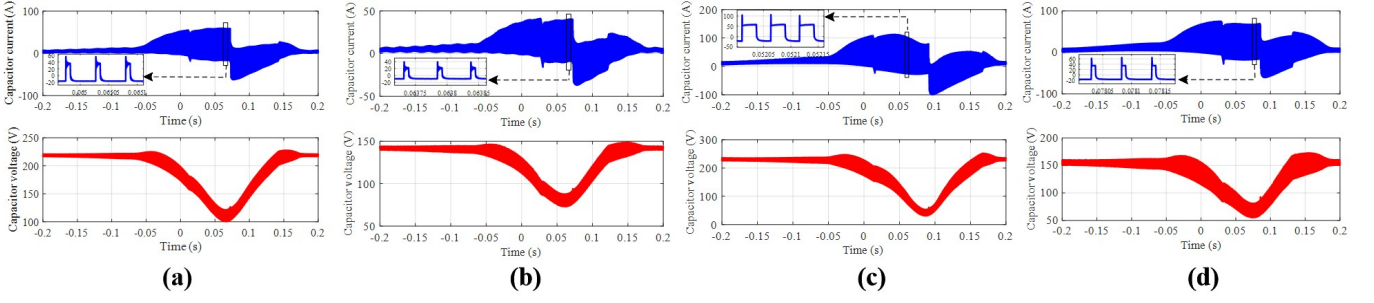


Fig. 8. (Color online) Measured capacitor current and voltage waveform. (a) 9-Caps, 500 A pulsed current; (b) 9-Caps, 300 A pulsed current; (c) 5-Caps, 500 A pulsed current; (d) 5-Caps, 300 A pulsed current.

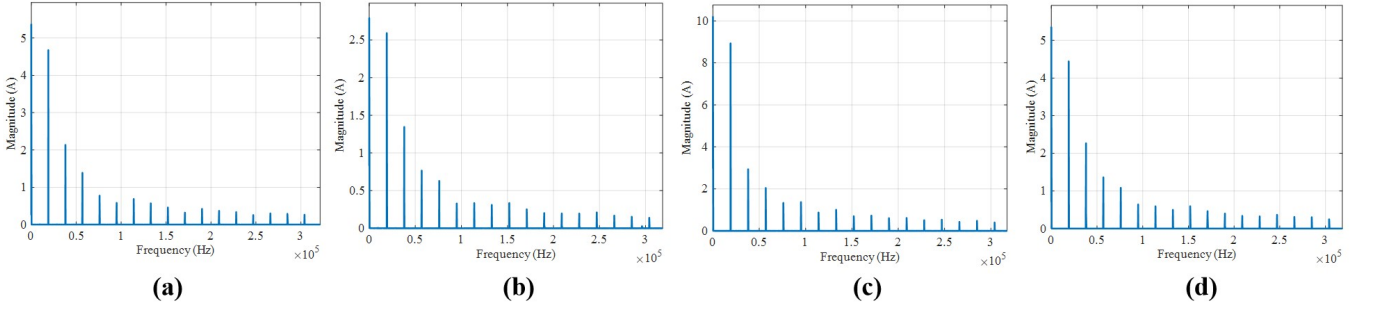


Fig. 9. FFT plots of capacitor current. (a) 9-Caps, 500 A pulsed current; (b) 9-Caps, 300 A pulsed current; (c) 5-Caps, 500 A pulsed current; (d) 5-Caps, 300 A pulsed current.

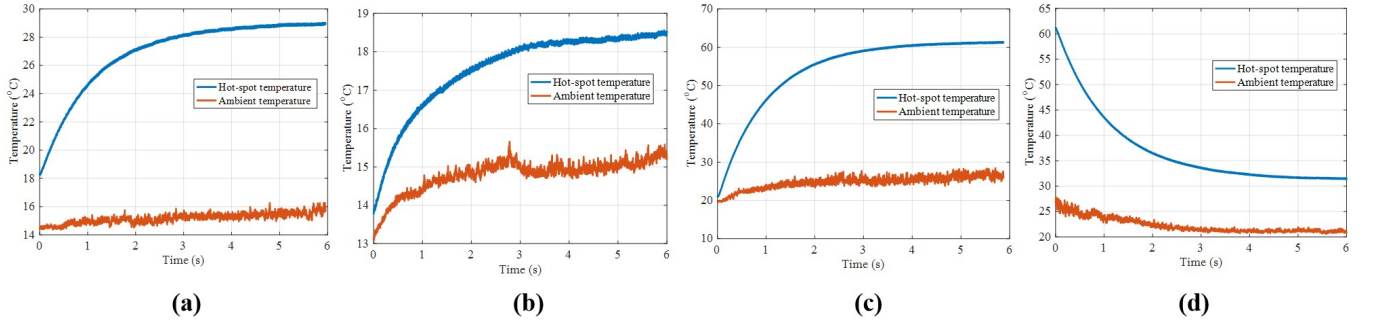


Fig. 10. (Color online) Measured hot spot temperature. (a) 9-Caps, 500 A pulsed current; (b) 9-Caps, 300 A pulsed current; (c) 5-Caps, 500 A pulsed current; (d) 5-Caps, 300 A pulsed current.

operating voltage V and operating hot-spot temperature T_h . The values of p_1 vary from 3 to 5, and $p_2 = 10$.

Owing to the differences in the actual capacitor manufacturing process, the lifetime calculated using a fixed-capacitor lifetime model has a large error. To solve this problem, Monte Carlo simulations are typically used to investigate the reliability of DC-link capacitors by considering the relevant parameter variations. This section considers two types of uncertainty [23]: 1) parameter uncertainty in applied lifetime models. The uncertainty of the fitting coefficient p_2 is considered; 2) parameter uncertainty between capacitors of the same product part number is considered. The difference between T_0 and T_h was considered. All parameters in the analysis were modeled using a normal probability distribution func-

tion. We assume that there is a 5% change in p_2 , L_0 , and T_h , with a confidence level of 90%. The specific parameters of the normal distribution are as follows:

$$\mu = \mu_{\text{test}}, \quad \sigma = \mu \times 5\%/z, \quad (22)$$

where μ_{test} is a fixed value for this parameter with a confidence level of 90% and $z = 1.65$.

When each parameter follows a normal distribution, the calculated capacitor lifetime also follows a normal distribution. To express the reliability of the capacitor more intuitively, the B1 lifetime is typically used, that is, the capacitor's lifetime when the capacitor's cumulative failure rate is 1% [29]. Table 7 lists the hot-spot temperature results for all capacitors under different experimental conditions. The DC-

Table 6. Comparison of calculation results and measurement results.

Condition	Flattop current (A)	Ambient temperature T_a ($^{\circ}\text{C}$)	Hot spot temperature T_h ($^{\circ}\text{C}$)	Experimental temperature rise ΔT_{exp} ($^{\circ}\text{C}$)	Estimated temperature rise ΔT_{est1} ($^{\circ}\text{C}$) (Measured icap)	Estimated temperature rise ΔT_{est2} ($^{\circ}\text{C}$) (Reconstructed icap)
9-Caps	500 A	15.8	28.9	13.1	13.0	13.4
	300 A	16.4	21.4	5.0	4.6	4.7
5-Caps	500 A	26.4	61.3	34.9	36.4	37.6
	300 A	20.9	31.1	10.2	10.1	10.4

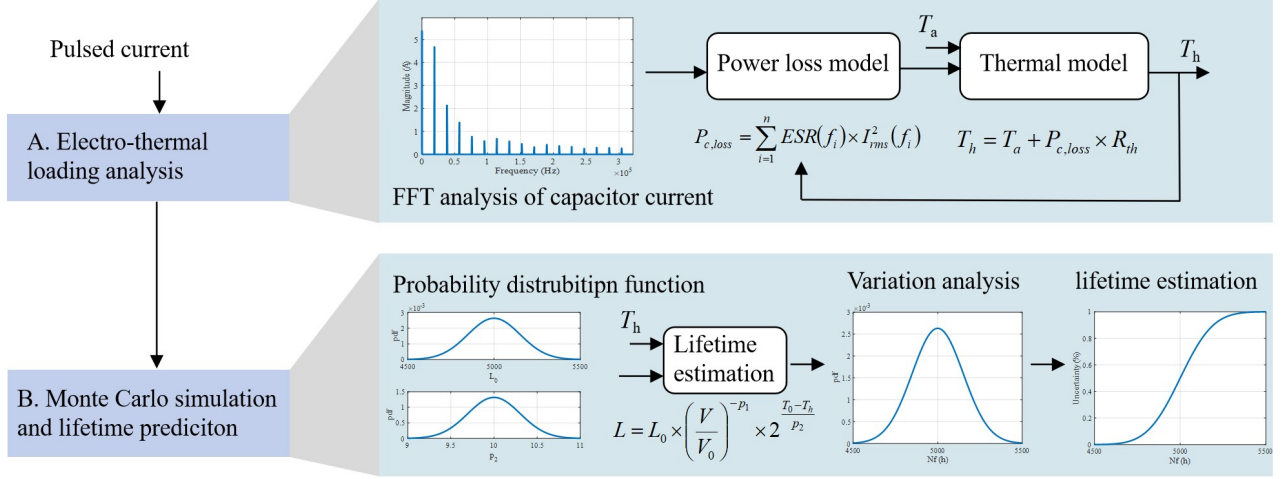


Fig. 11. Block diagram of DC-link capacitor lifetime evaluation.

link capacitors have different temperature distributions.

Figure 12(a), (b), (c), and (d) depict the B1 lifetime of capacitors under the condition of 300 A or 500 A pulsed current and 0.09 F or 0.05 F DC-link capacitance, respectively. The B1 lifetimes calculated from the estimated T_{hest1} and T_{hest2} values are also listed. Under the conditions of 300 A and 0.05 F, the B1 lifetimes of the five capacitors were 392, 411, 421, 460, and 489 days, respectively. When the number of DC-link capacitors was increased from five to nine, the lifetimes were 2.37 years, 2.43 years, 3.47 years, 2.50 years, 2.50 years, 2.54 years, 2.57 years, 2.62 years, and 2.66 years, respectively. Under the conditions of 500 A and 0.05 F, the B1 lifetimes of the five capacitors were 39, 42, 48, 56, and 60 days, respectively. When the number of capacitors is increased from 5 to 9, the lifetimes are 1.35 years, 1.40 years, 1.43 years, 1.46 years, 1.47 years, 1.55 years, 1.56 years, 1.56 years, and 1.68 years, respectively. It can be observed that connecting more capacitors in parallel can improve the lifetime of DC-link capacitors, and an imbalance of temperature in the capacitors can also lead to an imbalance in the lifetime.

B. Analysis and discussion

The hotspot temperature is a critical factor in the lifetime prediction scheme. The lifetime prediction of electrolytic capacitors in a pulsed power supply is limited to electrothermal stresses, and this study did not consider the failure mecha-

nism in terms of humidity. Accelerated testing of capacitors can be implemented under real operating conditions to obtain more accurate life-assessment results.

For small- and medium-power pulsed power supplies, such as quadrupole magnet power supplies and sextupole magnet power supplies, aluminum electrolytic capacitors are widely used as DC-link capacitors, whereas for high-pulsed power supplies, such as dipole magnet power supplies, film capacitors may be required [30]. Although this study focuses on aluminum electrolytic capacitors, the method applies to film capacitors. Film capacitors have a lower temperature increase than aluminum electrolytic capacitors owing to their low ESR over the entire frequency range. Film capacitors have the advantages of a long lifetime, high withstand voltage, high current tolerance, ability to withstand back pressure, high reliability, etc., and are expensive.

This study contributes to the design and maintenance of pulsed power supplies. During the design stage, the results of the capacitor lifetime assessment guide the design. During operation, devices that may fail can be replaced promptly to reduce maintenance costs.

VI. CONCLUSION

This study proposes a complete solution for the reliability evaluation of DC-link capacitor of a pulsed power supply. Based on the circuit model under different operating states, a

Table 7. The hot spot temperature measurement results of all DC-link capacitors under different conditions.

Condition	Hot spot temperature T_h ($^{\circ}\text{C}$)								
	Cap-1	Cap-2	Cap-3	Cap-4	Cap-5	Cap-6	Cap-7	Cap-8	Cap-9
500 A, 9-Caps	27.8	29.0	30.1	28.9	28.9	31.0	29.9	29.8	30.4
300 A, 9-Caps	21.2	21.7	22.3	21.8	21.4	22.9	22.1	22.1	22.5
500 A, 5-Caps	62.3	—	64.6	—	61.3	—	67.5	—	66.4
300 A, 9-Caps	32.0	—	33.3	—	31.1	—	34.3	—	33.6

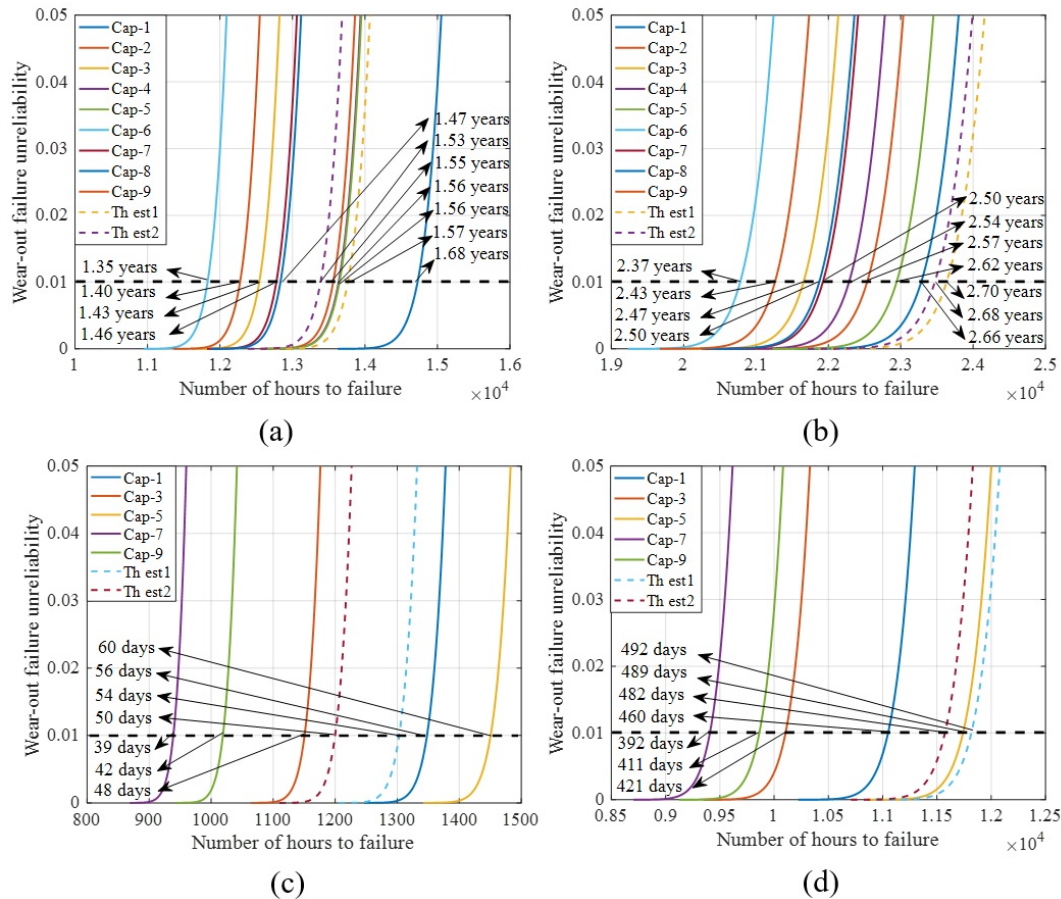


Fig. 12. (Color online) B1 Lifetime of DC-link capacitor under different conditions. (a) 9-Caps, 500 A pulsed current; (b) 9-Caps, 300 A pulsed current; (c) 5-Caps, 500 A pulsed current; (d) 5-Caps, 300 A pulsed current.

method for calculating the RMS value of the capacitor current is presented, and the accuracy of the method is verified. The proposed method does not require the establishment of a simulation model; it only requires analytical calculations based on the parameters, and the solution is quick and accurate. This study presents a capacitor current reconstruction method to measure the capacitor current without destroying

the connection structure. Electrothermal coupling analysis combined with FFT was used to calculate the hotspot temperature, which was experimentally verified with an error within 1.5°C . Lifetime prediction was carried out for all DC-link capacitors based on Monte Carlo analysis. Thus, the proposed method can be applied to film capacitors. This study contributes to the design of highly reliable pulsed power-supply systems.

[1] M. Yuichi, K. Yoshinori, M. Kazuki, et al., Capacitor bank of power supply for J-PARC MR main magnets. Nucl. Instrum. Meth. A. **901**, 156–163 (2018). doi:

10.1016/j.nima.2018.06.002

[2] R. Peron, F. Bordry, J. Burnet, et al., A 60MW pulsed power supply for particle accelerator: preliminary test results. EPE-

- PEMC 2010.(2010). doi:10.13140/2.1.5100.8643
- [3] R. Peron, V. Guennegues, J.L. Pouliquen, et al., Performances analysis of main components used in 60MW pulsed supply for particle accelerator. *Power Electronics and Applications*, 2009. EPE '09. 13th European Conference on. 1 - 10 (2009)
 - [4] X.H. Zhou, J.C. Yang, the HIAF project team, Status of the high-intensity heavy-ion accelerator facility in China. *AAPPS Bull.* **32**, 35 (2022). doi:10.1007/s43673-022-00064-1
 - [5] M.T. Tang, L.J. Mao, H.J. Lu, et al., Design of an efficient collector for the HIAF electron cooling system. *Nucl. Sci. Tech.* **32**, 116 (2021). doi: 10.1007/s41365-021-00949-0
 - [6] K.M. Yan, M.R. Li, Y.B. Zhou, et al., High-precision high-voltage detuning system for HIAF-SRing electron target. *Nucl. Sci. Tech.* **34**, 75 (2023). doi: 10.1007/s41365-023-01214-2
 - [7] Y. Li, F.J. Wu, X.J. Wang, et al., Structure and reliability design and experiment of HIAF-BRing dipole magnet pulse power supply. 2021 IEEE 1st International Power Electronics and Application Symposium (PEAS), 1-6 (2021), doi: 10.1109/PEAS53589.2021.9628550
 - [8] L.S. Peng, W.Z. Shen, A.H. Feng, et al., Method for obtaining junction temperature of power semiconductor devices combining computational fluid dynamics and thermal network. *Nucl. Instrum. Meth. A.* **976**, 164260 (2020). doi:10.1016/j.nima.2020.164260
 - [9] J. Wang, D.Q. Gao, W.Z. Shen, et al., Lifetime estimation of IGBT module using square-wave loss discretization and power cycling test. *Nucl. Sci. Tech.* **33**, 133 (2022). doi:10.1007/s41365-022-01118-7
 - [10] L.W. Zhou, B. Wang, Y. Zhang, et al., Review on Junction Temperature Management of Power Semiconductor Devices Under Power Fluctuation Condition. *Proceedings of the CSEE* **33**, 2394-2407+2549 (2018). doi: 10.13334/j.0258-8013.pcsee.171721. (in Chinese)
 - [11] H. Wang, F. Blaabjerg, Reliability of capacitors for DC-link applications in power electronic converters—An Overview. *IEEE T. Industrial Appl.* **50**, 3569-3578 (2014). doi: 10.1109/TIA.2014.2308357
 - [12] W.J. Tang, K. Yao, W.B. Hu, et al., An Online Monitoring Scheme of Output Capacitor's ESR and C for CCM Buck Converters Without Current Sensors. *Proceedings of the CSEE* **35**, 5569-5576 (2015). doi: 10.13334/j.0258-8013.pcsee.2015.21.021. (in Chinese)
 - [13] H.C. Zhu, H. Wang, S.T. Gao et al., Quasi-online Condition Monitoring Method of DC-Link Capacitor of Wind Power Converter. *High Voltage Engineering* **49**, 373-381 (2023). doi: 10.13336/j.1003-6520.hve.20211413. (in Chinese)
 - [14] S.S. Ahmad, G. Narayanan, Evaluation of DC-Link Capacitor RMS Current in Switched Reluctance Motor Drive. *IEEE T. Industrial Appl.* **57**, 1459-1471 (2021), doi: 10.1109/TIA.2020.3048637
 - [15] Y.F. Huang, S. Xu, H.F. Wang, et al., Analytical Calculation of Ripple Current on DC-Link Capacitor for Brushless DC Motor Square Wave Control System. *Transactions of China Electrotechnical Society* **33**, 4544-4552 (2018). doi: 10.19595/j.cnki.1000-6753.tces.171217. (in Chinese)
 - [16] J.W. Kolar, T.M. Wolbank, M. Schrodli, Analytical calculation of the RMS current stress on the DC-link capacitor of voltage PWM converter systems. 1999. Ninth International Conference on Electrical Machines and Drives. 81-89 (1999), doi: 10.1049/cp:19990995
 - [17] M. Chai, C.M. Tu, B. Xiao, et al., Study on Modeling and Thermal Behavior of Spiral Wound Aluminum Electrolytic Capacitor. 2020 IEEE 4th Conference on Energy Internet and Energy System Integration (EI2). 1337-1342 (2020), doi: 10.1109/EI250167.2020.9347361
 - [18] B. Yao, Reliability evaluation of dc-link capacitor banks in the high-speed train traction drive system,(2020). doi: 10.27414/d.cnki.gxnju.2020.000768.(in Chinese)
 - [19] H. Niu, Mission profile based reliability assessment and optimization design of switching mode power supply,(2021). doi: 10.27061/d.cnki.ghgdu.2021.000522.(in Chinese)
 - [20] B. Yao, X.L. Ge, H.M. Wang, et al., Multiscale Reliability Evaluation of DC-Link Capacitor Banks in Metro Traction Drive System.in *IEEE Transactions on Transportation Electrification* **6**, 213-227 (2020). doi: 10.1109/TTE.2020.2974182
 - [21] Y.H. Yang, K. Ma, H. Wang, et al., Mission profile translation to capacitor stresses in grid-connected photovoltaic systems. 2014 IEEE Energy Conversion Congress and Exposition (ECCE), 5479-5486 (2014), doi: 10.1109/ECCE.2014.6954152
 - [22] H.Q. Wen, W.D. Xiao, X.H. We, et al., Analysis and evaluation of DC-link capacitors for high-power-density electric vehicle drive systems. *IEEE Transactions on Vehicular Technology* **61**, 2950-2964 (2012). doi: 10.1109/TVT.2012.2206082
 - [23] H.R. Wang, P. Davari, H. Wang, et al., Lifetime Estimation of DC-Link Capacitors in Adjustable Speed Drives Under Grid Voltage Unbalances. *IEEE. T. Power. Electr.* **34**, 4064-4078 (2019). doi: 10.1109/TPEL.2018.2863701
 - [24] Z.Y. Zhao, P. Davari, W.G. Lu, et al., An Overview of Condition Monitoring Techniques for Capacitors in DC-Link Applications. *IEEE. T. Power. Electr.* **36**, 3692-3716 (2021). doi: 10.1109/TPEL.2020.3023469
 - [25] Z.Y. Zhao, W.G. Lu, P. Davari, et al., An online parameters monitoring method for Output capacitor of buck converter based on large-signal load transient trajectory analysis. *IEEE Journal of Emerging and Selected Topics in Power Electronics* **9**, 4004-4015 (2021). doi: 10.1109/JESTPE.2020.2964068
 - [26] M.D. Singh, K.B. Khanchandani, *Power Electronics*, 2nd edn. (Tsinghua University Press, 2011), pp. 491-495
 - [27] W.Z. Shen, H.B. Yan, D.Q. Gao, et al., Simulation and implementation of scanning magnet power supply. *Nuclear techniques* **37**, 47-50 (2014). (in Chinese)
 - [28] H. Niu, H. Wang, X. Ye, et al., Converter-level FEM simulation for lifetime prediction of an LED driver with improved thermal modelling. *Microelectronics Reliability* **76-77**, 117-122 (2017). doi: 10.1016/j.microrel.2017.06.079
 - [29] H. Niu, S. Wang, X. Ye, et al., Lifetime prediction of aluminum electrolytic capacitors in LED drivers considering parameter shifts. *Microelectronics Reliability* **88-90**, 453-457 (2018). doi: 10.1016/j.microrel.2018.06.027
 - [30] Y. Li, F.J. Wu, Y.Z. Huang, et al., High voltage and low voltage switching control and switching point smoothing algorithm of HIAF-BRing fast cycle full energy storage pulse power supply. *High Power Laser and Particle Beams* **35**, 79-87 (2023). doi: 10.11884/HPLPB202335.230037. (in Chinese)